Supporting Information

Bifunctional citrate-$Ni_{0.9}Co_{0.1}(OH)_x$ layer coated fluorine-doped hematite for simultaneous hole extraction and injection towards efficient photoelectrochemical water oxidation

Peng Wang[a], Feng Li[b], Xuefeng Long[c], Tong Wang[a], Huan Chai[a], Honglei Yang[a], Shuwen Li[a], Jiantai Ma[a], Jun Jin[a,*]

[a] *State Key Laboratory of Applied Organic Chemistry (SKLAOC), The Key Laboratory of Catalytic Engineering of Gansu Province, College of Chemistry and Chemical Engineering, Lanzhou University, Lanzhou, Gansu, 730000 (P. R. China)*

[b] *State Key Laboratory of High-efficiency Utilization of Coal and Green Chemical Engineering, College of Chemistry and Chemical Engineering, Ningxia University, Yinchuan, Ningxia, 750021 (P. R. China)*

[c] *College of Petrochemical Technology, Lanzhou University of Technology, Langongping Road 287, Lanzhou 730050 (P. R. China)*

*Corresponding author: jinjun@lzu.edu.cn

Materials and Reagents

$FeCl_3 \cdot 6H_2O$ and urea were purchased from Aladdin Industrial Corporation. KOH and Na_2SO_3 were purchased from Sinopharm Chemical Reagent Co., Ltd. $Co(NO_3)_2 \cdot 6H_2O$, $Ni(NO_3)_2 \cdot 6H_2O$, and sodium citrate were purchased from Tianjin Guanghua Technology Development Co., Ltd. Deionized (DI) water (18.2 MΩ cm) used in this work was obtained from a Molecular Lab water purifier. Before the experiments, fluorine-doped tin oxide-coated glass (FTO, < 15 Ω sq^{-1}, Nippon Sheet Glass Co., Ltd.) was cut into 1 × 2.5 cm and was ultrasonically cleaned with acetone, ethanol and DI water for 20 min each. All reagents above were analytical grade and were used without further purification.

Characterizations

The morphology of all photoanodes were characterized by a field emission scanning electron microscopy (SEM; Hitachi S-4800). Transmission electron microscopy (TEM) and high-resolution TEM (HRTEM) associated with an X-ray energy-dispersive spectrometer (EDS) were analyzed on a Tecnai G^2Tf20 transmission operated at 200 kV. The crystallization was studied by the X-ray diffraction spectra (XRD), conducted on a Rigaku D/max-2400 diffractometer with the X-ray source of Cu Kα radiation and data were collected in Bragg–Brentano mode with a scan rate of 0.2^o s^{-1} in the range of 10^o-90^o. The surface bonding information was analyzed by X-ray photoelectron spectroscopy (XPS) measurements, operated on a Kratos Axis Nova X-ray photoelectron spectrometer with a monochromated Al Kα X-ray source, operating at 15 kV and 10 mA and referenced to the C 1s peak (284.8 eV). Raman spectra were researched Via Renishaw confocal spectroscopy with 633 nm laser excited, and the sample side of photoanode faced the laser source. The light absorption abilities of all samples were measured with UV/Vis absorption spectra (Hitachi U-4000) with $BaSO_4$ as the reference.

Photoelectrochemical (PEC) measurements

The PEC measurements of all photoanodes were achieved on the CHI760E electrochemical workstation (CH Instruments Co.) in a standard three-electrode system, which containing the photoanodes (WE), a Pt fossil (1 × 1 cm^2, CE), a saturated Ag/AgCl electrode (RE). All PEC measurements were performed in the 1 M KOH electrolyte (PH=13.6), and the effective work area of the photoanodes was adjusted to 1 cm× 1 cm^2. A 300 W xenon arc lamp (Perfect Light solar simulator) equipped with an AM 1.5 G filter was employed as the light source, and the light intensity on the electrode surface was adjusted to 100 mW cm^{-2} (1 sun illumination). Linear sweep voltammetry curves were obtained with a scan rate of 5 mV s^{-1} in the potential range of 0.5 V~1.6 V vs. RHE. A monochromator was utilized to measure the incident photon-to-current efficiency (IPCE) with a 300 W Xe lamp as the

simulated light source. Mott-Schottky (M-S) curves were gained at the dark condition and with a fixed frequency of 1 kHz with a scan rate of 20 mV^{-1}. Electrochemical impendence spectroscopy (EIS) was obtained at a 1.23 V vs. RHE under light with an ac voltage amplitude of 5 mV over a frequency range from 10^{-1} to 10^{6} Hz, and was fitted by ZView software.

Equations in this work

1. The measured potential was converted to the reversible hydrogen electrode (RHE) using the Nernst equation:

$$E_{RHE} = E_{Ag/AgCl} + E^{0}_{Ag/AgCl} + 0.0591\ V \times pH \qquad \textbf{equation S1}$$

Where E_{RHE} is the converted potential vs. RHE, $E_{Ag/AgCl}$ is experimentally measured potential against Ag/AgCl reference electrode, and $E^{0}_{Ag/AgCl} = 0.1976$ V (vs. Ag/AgCl) at 25 ℃.[1]

2. Calculation of the Applied bias photo-to-current conversion efficiency (ABPE)

Assuming 100% Faradaic efficiency, the ABPE was obtained by the following equation:

$$ABPE\ (\%) = [J \times (1.23 - E_{app})/P_{light}\ ] \times 100\% \qquad \textbf{equation S2}$$

Where J is the measured photocurrent density (mA cm^{-2}), E_{app} is the applied potential (V vs. RHE) and P_{light} is the incident illumination power density (100 mW cm^{-2}).

3. Calculation of the Incident photo-to-electron conversion efficiency (IPCE):

$$IPCE(\%) = [(J_{mono} \times 1240) / (\lambda \times P_{mono})] \times 100\% \qquad \textbf{equation S3}$$

where J_{mono} is the measured photocurrent density at the specific measurement wavelength (mA cm^{-2}), λ is the incident light wavelength (nm) and P_{mono} is the measured irradiance at the specific measurement wavelength (mW m^{-2}).

4. Electrochemical double layer capacitance (C_{dl})

The electrochemically active surface area (EASA) was estimated from the electrochemical double-layer capacitance. Cyclic voltammograms were performed at

the scan rate of 20, 40, 60, 80, 100, 120, 140, 160, 180, 200 mV s^{-1} (Fig. S8). Then the EASA was determined by measuring the capacitive current associated with double-layer charging from the scan-rate dependence of CVs. The double layer capacitance (C_{dl}) was estimated by plotting the $\triangle J = (J_a - J_c)$ at 1.23 V vs. RHE against the scan rate as shown in Fig. 3d, where J_a and J_c are the anodic and cathodic current, respectively. The linear slope is twice of the C_{dl}, which can be used to represent the EASA.[2]

5. Mott-Schottky measurement

M-S plots were collected at an AC frequency of 1kHz in the dark, and the N_D of the photoanodes could be estimated by the following equation:

$$N_D = \frac{2}{e\varepsilon\varepsilon_0}\left[\frac{d(\frac{1}{C^2})}{dV}\right]^{-1} \quad \textbf{equation S4}$$

Where C is the space charge capacitance in the semiconductor (obtained from M-S curves), e is the electron charge, ε is the vacuum permittivity (8.85×10^{-12} F m^{-1}), ε_0 is the relative dielectric constant of hematite ($\varepsilon_0 = 80$),[3] N_D is the charge donor density (cm^{-3}), V is the electrode applied potential, V_{fb} is the flat band potential, κ is the Boltzmann's constant (1.38×10^{-23} J K^{-1}) and T is the absolute temperature (K). It should be noted that the capacitance (C) is based on a flat structure, and therefore it is not suitable for our non-flat structure of the one-dimensional geometry nanorod arrays. In general, the comparison results of the flat structure and non-flat structure show that an underestimate of the donor density by 20% is achieved for the latter mode when it is considered as the former one. In this work, all the Fe_2O_3-based nanoarrays photoanodes are non-flat structure, thus the N_D values for them are 20% larger than the experimental results calculated by equation.

6. Light harvesting efficiency (LHE)

LHE is defined as the fraction of photons absorbed per photons impinging on the sample, which could be calculated using the following equation:

$$LHE = 1 - 10^{-A(\lambda)} \quad \textbf{equation S5}$$

A(λ) is the absorbance at a specific wavelength.

7. Theoretical maximum photocurrent density (Jabs)

Theoretical maximum photocurrent density (J_{abs}) is the photocurrent density assuming that all absorbed photons can be converted into current (i.e., APCE = IPCE/LHE = 100%), it is a constant with the AM 1.5G spectrum and the light harvesting efficiency of the fixed photoelectrode. In the case of J_{abs}, it can be calculated according to the following equation:

$$J_{abs} = \int_{\lambda_1}^{\lambda_2} \frac{\lambda \times LHE(\lambda) \times P(\lambda)}{1240} d(\lambda)$$

equation S6

where λ and P(λ) are the light wavelength (nm) and the corresponding power density (mW cm^{-2} nm^{-1}) for the standard solar spectrum AM 1.5G (ASTMG-173-03), respectively.

8. The surface charge injection efficiency ($\eta_{surface}$) and bulk charge separation efficiency (η_{bulk})

Photocurrent density arising from PEC water oxidation can be described by the following equation：

$$J_{H_2O} = J_{abs} \times \eta_{bulk} \times \eta_{surface}$$

equation S7

η_{bulk} is the yield of photo-induced holes which have migrated to the semiconductor/electrolyte interfaces and $\eta_{surface}$ is the yield of holes which are involved in water oxidation reaction. In this work, we chose the widely used Na_2SO_3 as the hole scavenger. Moreover, η_{bulk} and $\eta_{surface}$ were calculated according to the equations, respectively：

$$\eta_{bulk} = \frac{J_{Na_2SO_3}}{J_{abs}} \quad ,$$

equation S8

$$\eta_{surface} = \frac{J_{H_2O}}{J_{Na_2SO_3}}$$

equation S9

$J_{Na_2SO_3}$ and J_{H_2O} are the photocurrent densities measured in 1M KOH with and without 1 M Na_2SO_3, respectively.

9. The transient decay time

The transient decay time of the photoanodes were calculated according to the transient photocurrent curves in Fig. 5c by the following equation:

$$D=(I_t-I_s)/(I_m-I_s) \qquad \textbf{equation S10}$$

where I_t represents current at time. The transient decay time is defined as the time at which ln D = -1.

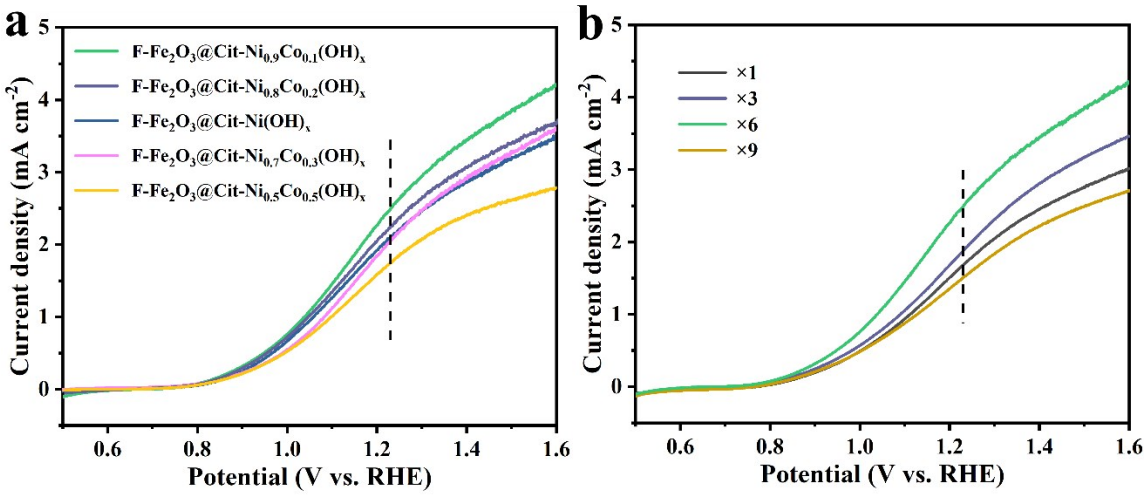

Fig. S1. LSV curves of (a) the composite photoanodes with different Co/Ni ratios and (b) the F-Fe_2O_3@Cit-$Ni_{0.9}Co_{0.1}(OH)_x$ synthesized with different spin-coating times.

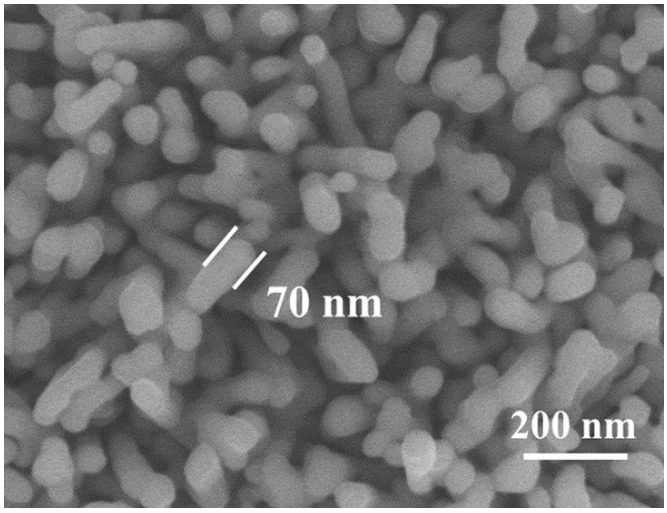

Fig. S2. SEM image of α-Fe_2O_3 NAs.

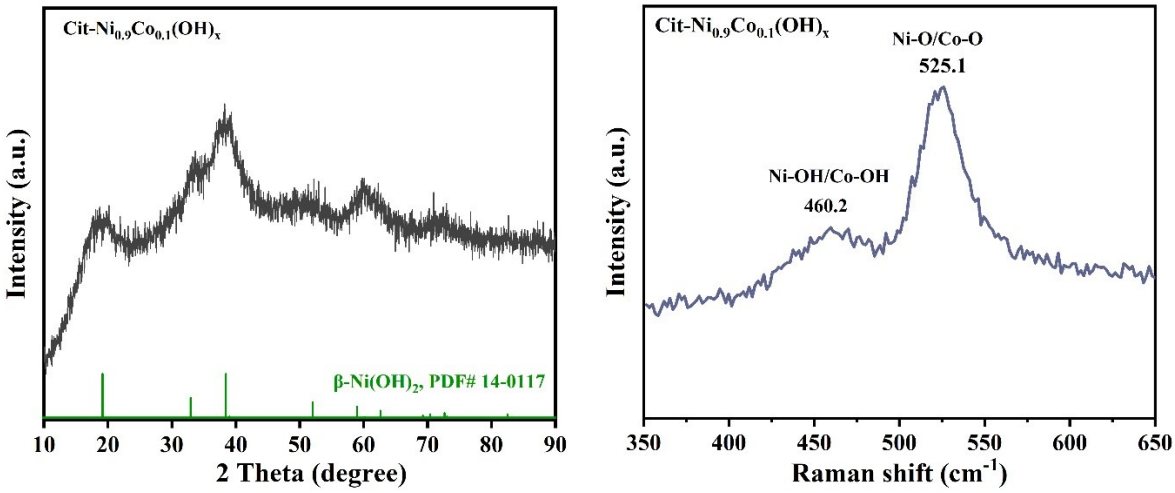

Fig. S3. (a) XRD pattern and (b) Raman spectra of Cit-$Ni_{0.9}Co_{0.1}(OH)_x$ powder.

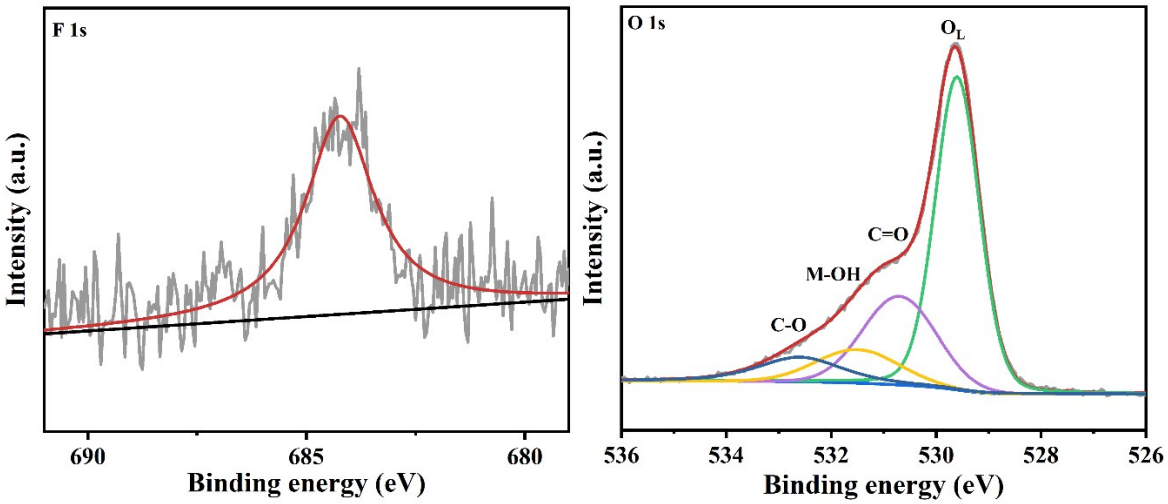

Fig. S4. (a) F 1s and (b) O 1s high-resolution XPS spectra of F-Fe_2O_3@Cit-$Ni_{0.9}Co_{0.1}(OH)_x$

photoanode.

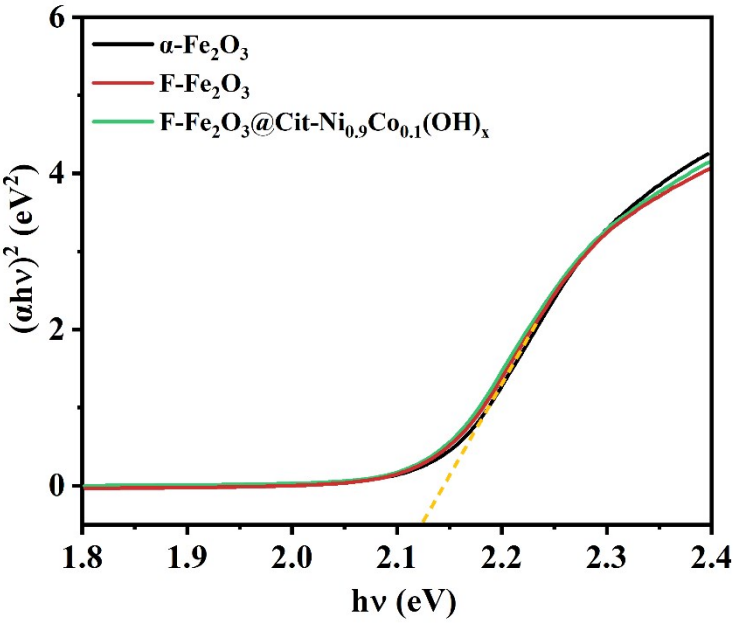

Fig. S5. Fitted band-gaps of α-Fe_2O_3, F-Fe_2O_3 and F-Fe_2O_3@Cit-$Ni_{0.9}Co_{0.1}(OH)_x$.

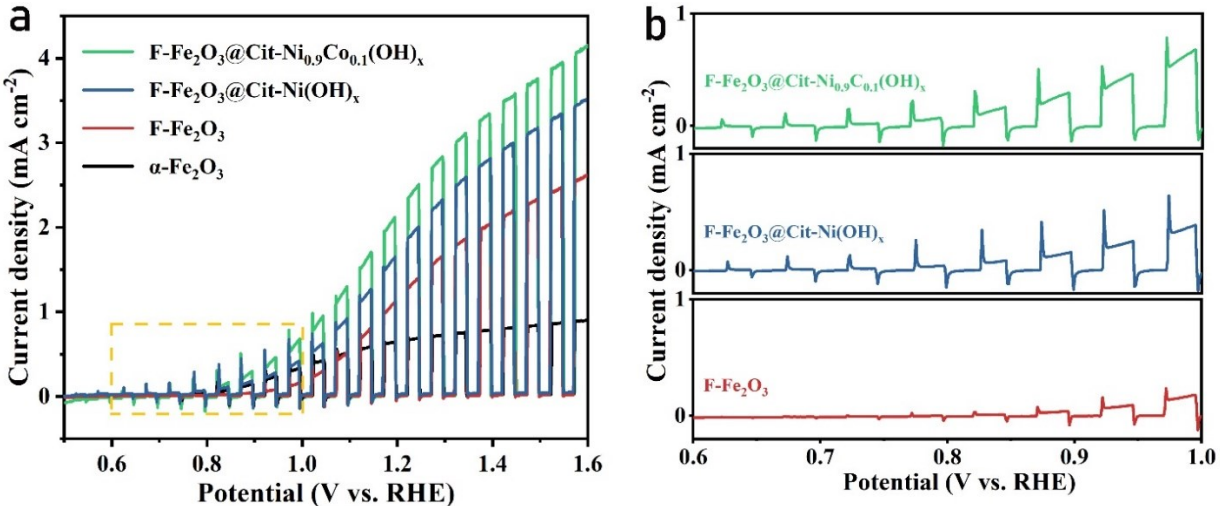

Fig. S6. (a) LSV curves under chopped illumination at 0.5~1.6 V vs. RHE and (b) an enlarged range of 0.6~1.0 V vs. RHE.

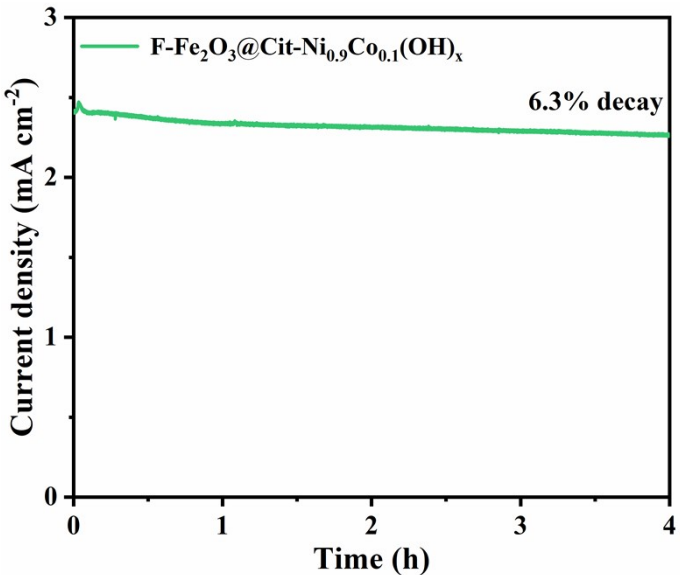

Fig. S7. Chronoamperometry curve of the target F-Fe_2O_3@Cit-$Ni_{0.9}Co_{0.1}(OH)_x$ photoanode at 1.23 V vs. RHE.

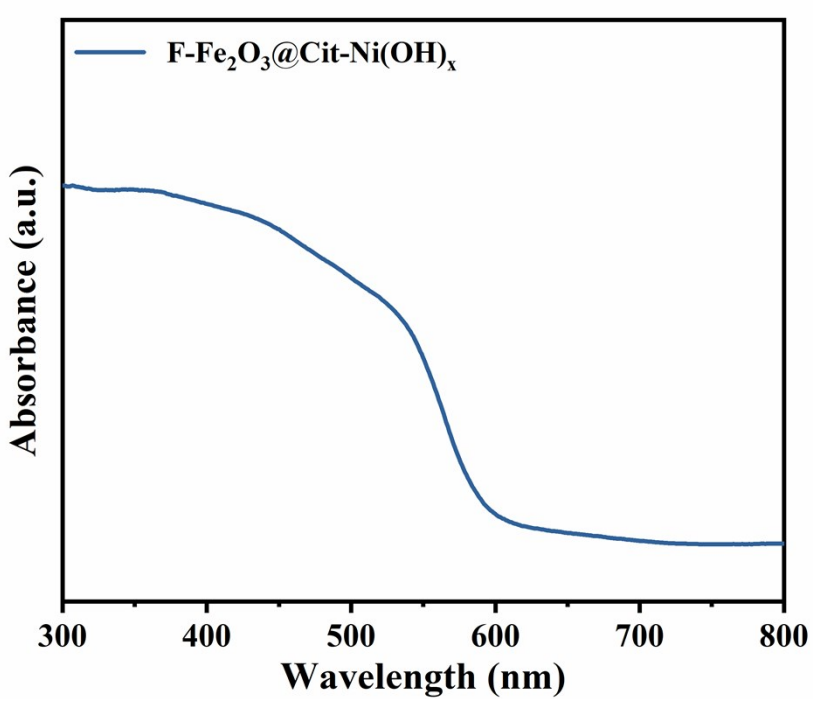

Fig. S8. UV-visible absorption spectra of F-Fe_2O_3@Cit-Ni$(OH)_x$ photoanode.

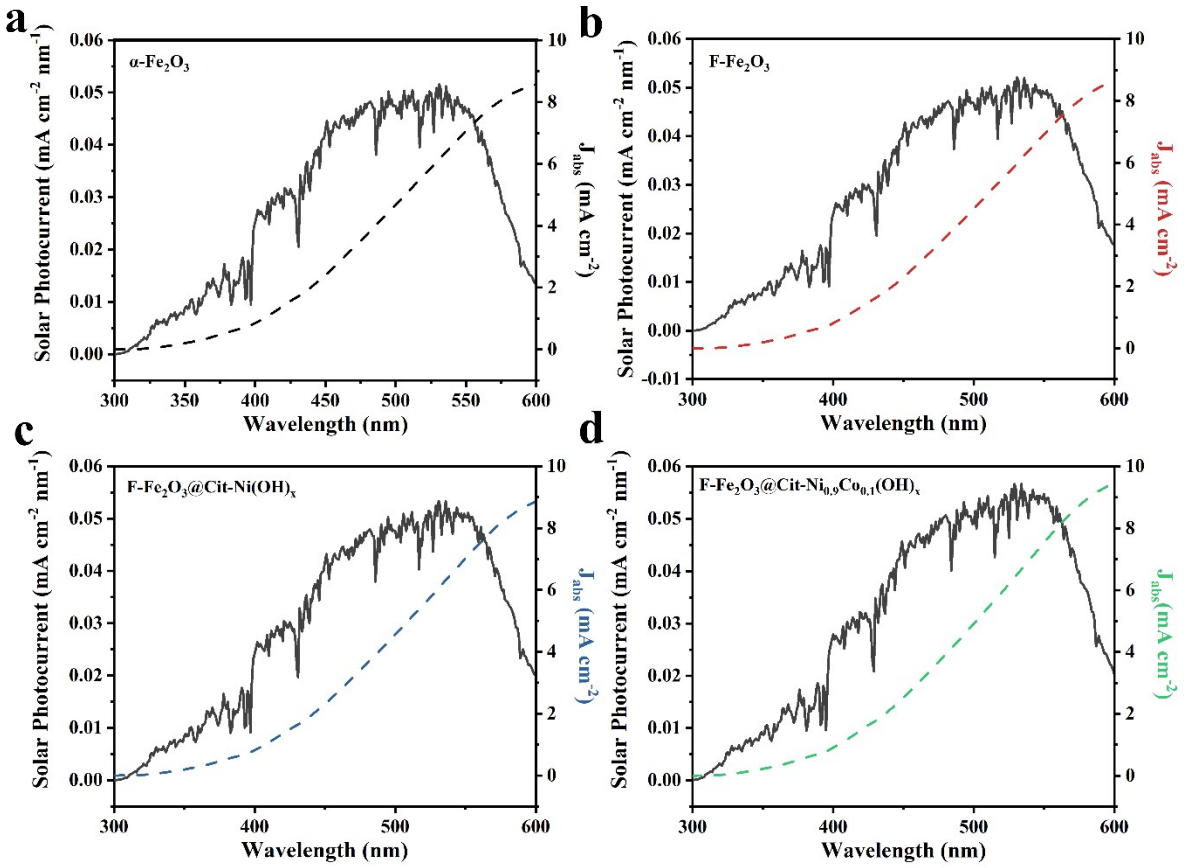

Fig. S9. J_{abs} of (a) α-Fe_2O_3, (b) F-Fe_2O_3, (c) F-Fe_2O_3@Cit-$Ni(OH)_x$, (d) F-Fe_2O_3@Cit-$Ni_{0.9}Co_{0.1}(OH)_x$ photoanodes (assuming 100% absorbed photo-to-current conversion efficiency for photons).

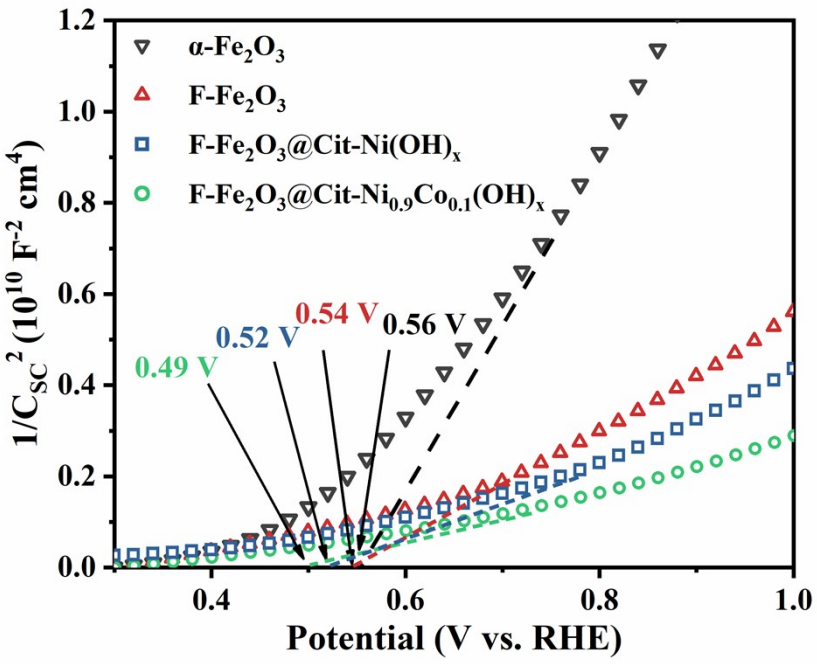

Fig. S10. Mott-Schottky plots of all as-prepared photoanodes.

Mott-Schottky (M-S) analysis was conducted at a fixed frequency of 1kHz in dark. Donor density (N_D) was evaluated from the slopes of the normalized M-S plots by equation S4, and the flat-band potentials were estimated from x-axis intercept. Fig. S10 clearly shows that all photoanodes own the typical positive slopes of n-type semiconductors, with the electrons as the majority charge carriers. The flat-band potentials present a trend of gradual cathodic shift from α-Fe_2O_3 to the target photoanode. The N_D value increases dramatically from 5.14×10^{19} cm^{-3} to 1.93×10^{20} cm^{-3} after doping with F, suggesting that fluorine anion acts as a promising n-type dopant to largely enhance the carrier concentration of the hematite. After encapsulating F-Fe_2O_3 with the surface overlayers, the N_D values of the composite photoanodes slightly increase to 2.72×10^{20} cm^{-3} and 3.59×10^{20} cm^{-3} for F-Fe_2O_3@Cit-$Ni(OH)_x$ and F-Fe_2O_3@Cit-$Ni_{0.9}Co_{0.1}(OH)_x$, respectively.

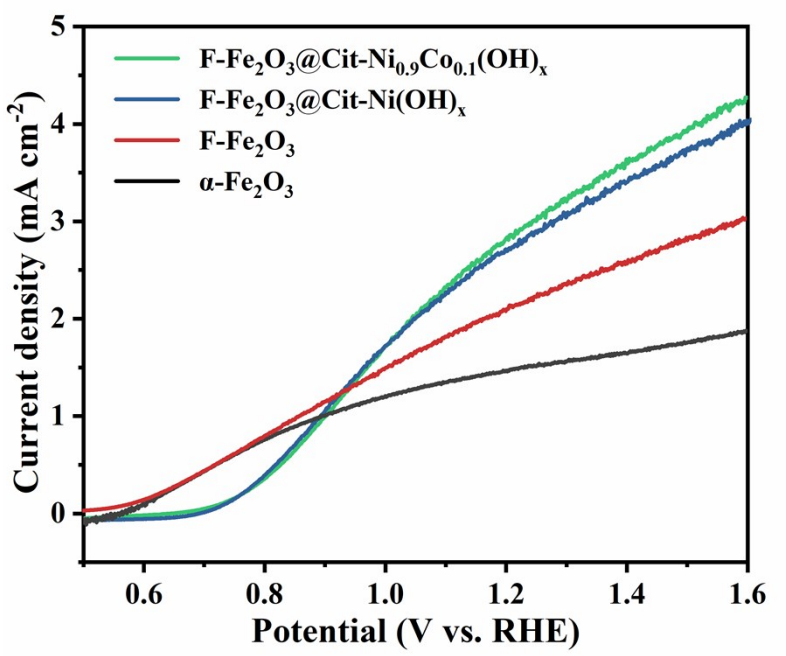

Fig. S11. LSV curves collected in 1 M Na_2SO_3+1 M KOH electrolyte.

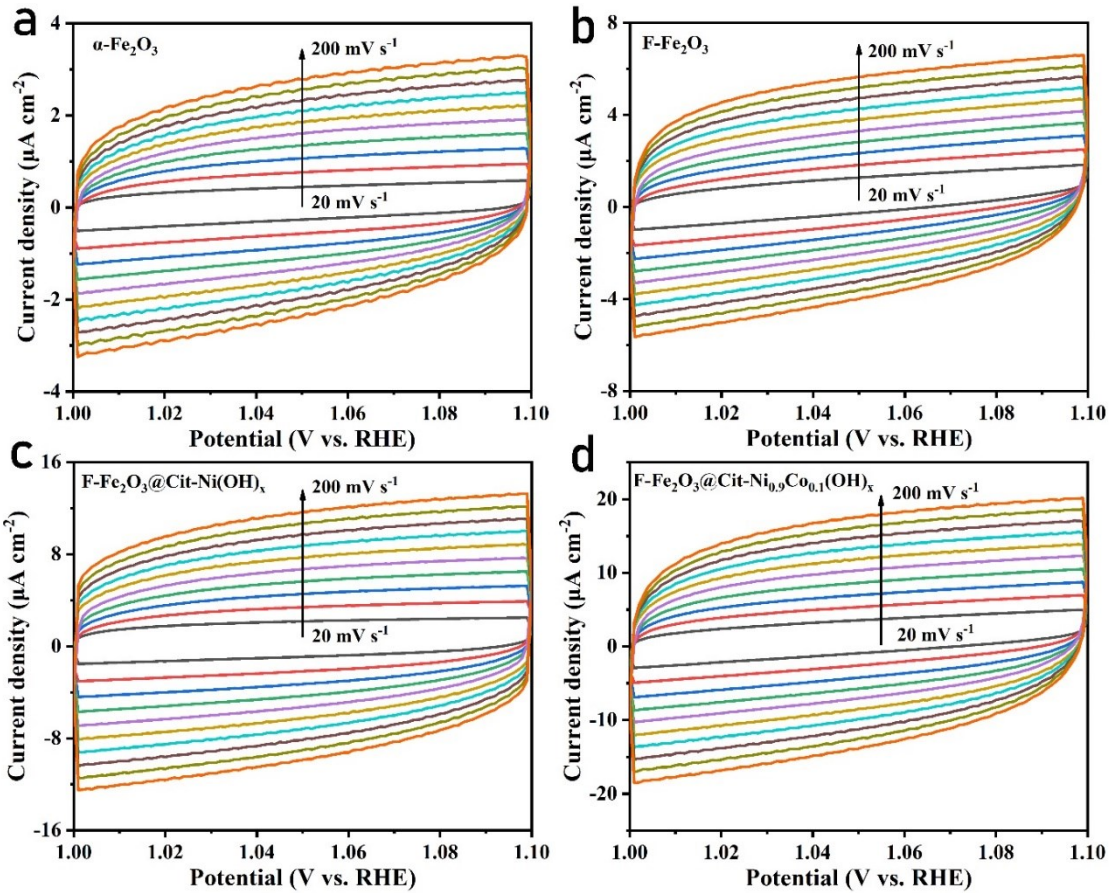

Fig. S12. Voltammograms of (a) α-Fe_2O_3, (b) F-Fe_2O_3, (c) F-Fe_2O_3@Cit-$Ni(OH)_x$ and (d) F-Fe_2O_3@Cit-$Ni_{0.9}Co_{0.1}(OH)_x$ photoanodes at various scan rates (20-200 mV s^{-1}) .

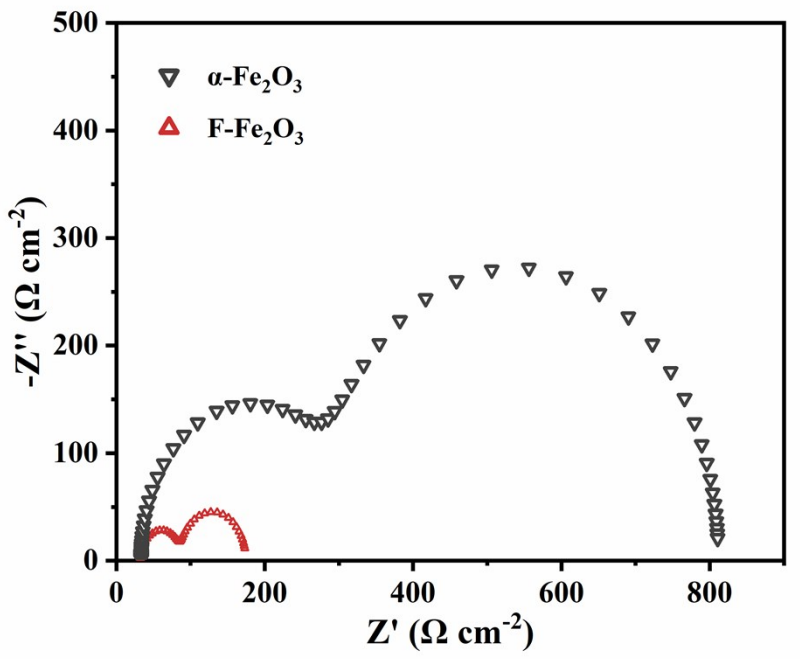

Fig. S13. Comparison of Nyquist plots of α-Fe_2O_3 and F-Fe_2O_3 photoanodes.

Table S1. The fitted resistances of the photoanodes.

Sample	R_{trap} (Ω cm^{-2})	R_{ct} (Ω cm^{-2})
F-Fe_2O_3@Cit-$Ni_{0.9}Co_{0.1}(OH)_x$	32.7	51.3
F-Fe_2O_3@Cit-$Ni(OH)_x$	38.1	85.7
F-Fe_2O_3@Cit-$Co(OH)_x$	44.2	65.9
F-Fe_2O_3	56.5	86.4
α-Fe_2O_3	236.4	540.6

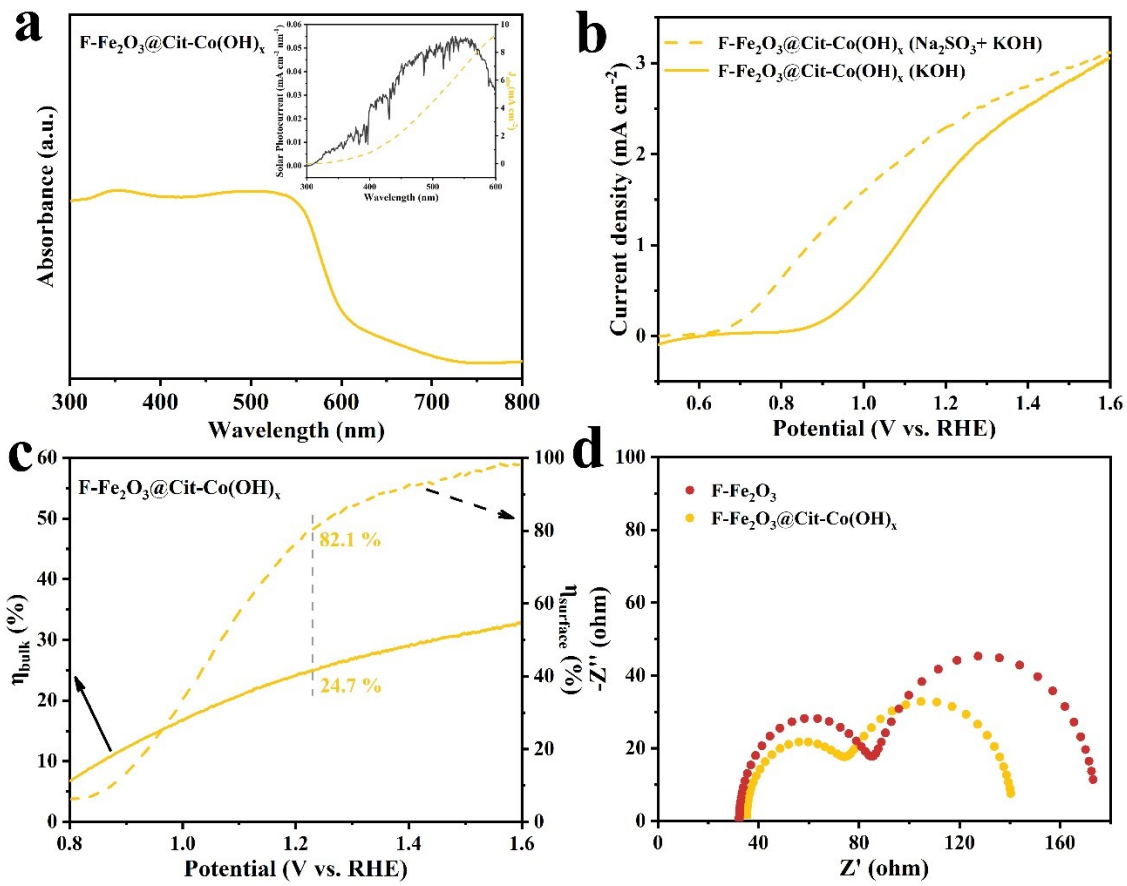

Fig. S14. (a) UV-visible absorption spectra (inset: J_{abs} of the F-Fe_2O_3@Cit-$Co(OH)_x$ photoanode), (b) LSV curves collected in 1M KOH and in 1M Na_2SO_3+ 1M KOH and (c) bulk charge separation efficiency and surface charge transfer efficiency of the F-Fe_2O_3@Cit-$Co(OH)_x$ photoanode; (d) the comparison of Nyquist plots between the F-Fe_2O_3 and F-Fe_2O_3@Cit-$Co(OH)_x$ photoanodes.

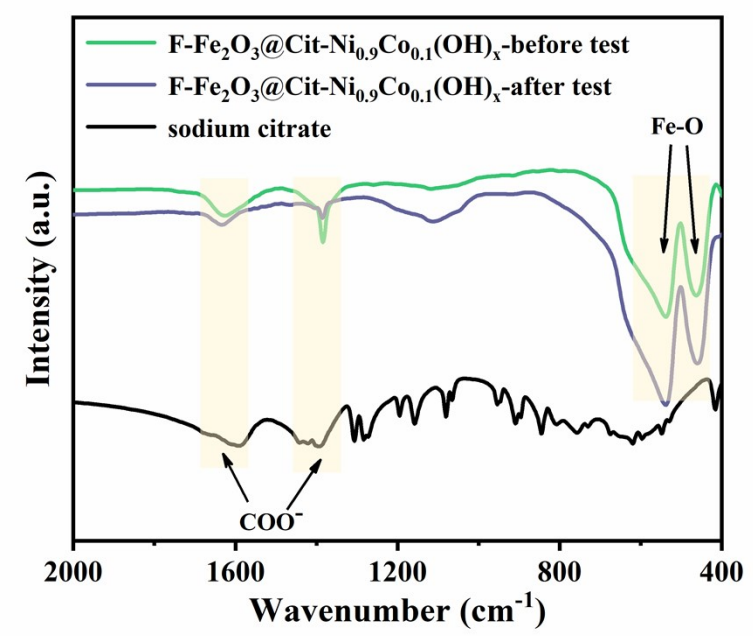

Fig. S15. FT-IR spectra of F-Fe_2O_3@Cit-$Ni_{0.9}Co_{0.1}(OH)_x$ photoanode (before and after long-term stability test) and sodium citrate.

Fourier-transform infrared (FT-IR) spectra of the target photoanode (before and after 4h-stability test) and sodium citrate suggest the existence of citrate anion in F-Fe_2O_3@Cit-$Ni_{0.9}Co_{0.1}(OH)_x$. As shown in Fig. S14, the peaks at 1589 cm^{-1} and 1386 cm^{-1} could be ascribed to the asymmetric vibration and symmetric vibration of COO^- of citrate anion,[4] while the two sharp peaks of 539 cm^{-1} and 460 cm^{-1} are Fe-O stretching and bending peaks of crystalline hematite.[5]

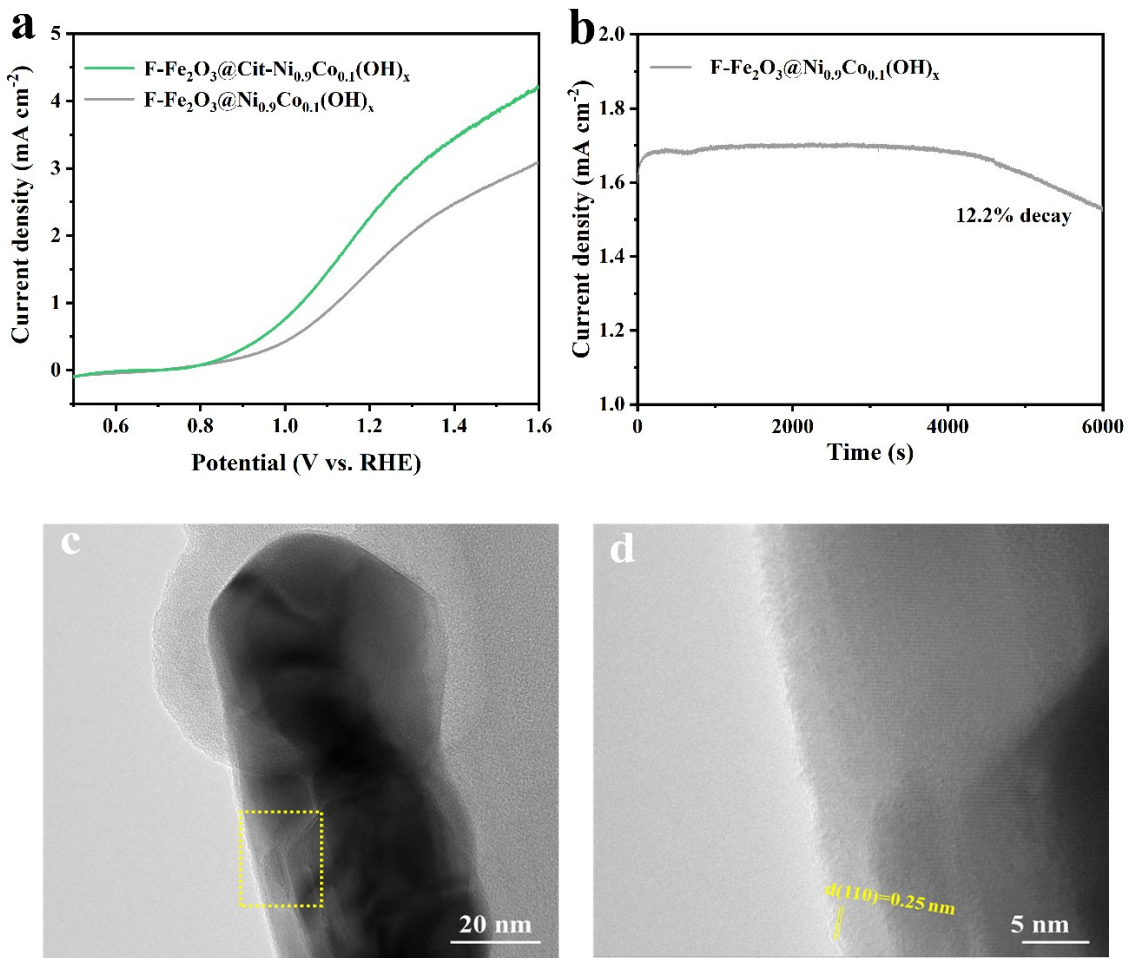

Fig. S16. (a) Comparison of LSV curves of F-Fe_2O_3@Cit-$Ni_{0.9}Co_{0.1}(OH)_x$ and F-Fe_2O_3@$Ni_{0.9}Co_{0.1}(OH)_x$; (b) Chronoamperometry curve of the F-Fe_2O_3@$Ni_{0.9}Co_{0.1}(OH)_x$ photoanode; (c) TEM and (d) HRTEM images of the F-Fe_2O_3@$Ni_{0.9}Co_{0.1}(OH)_x$ photoanode after the 6000s-photostability test.

Table S2. A comparison of the target F-Fe_2O_3@Cit-$Ni_{0.9}Co_{0.1}(OH)_x$ photoanode in this work with previously reported Fe_2O_3-based photoanodes for PEC water oxidation.

Composite photoanode	The onset potential (V vs. RHE)	Current density at 1.23 V vs. RHE	IPCE (%) at 1.23 V vs. RHE	Reference
F-Fe_2O_3@Cit-$Ni_{0.9}Co_{0.1}(OH)_x$	0.79	2.52 mA cm^{-2}	40 (300 nm)	This work
Fe@Ni-MOF/Fe_2O_3:Ti	0.7	2.3 mA cm^{-2}	34.2 (350 nm)	6
Fe_2O_3/$Fe_{0.5}Mn_{0.5}OOH$	~0.4	3.36 mA cm^{-2}	no	7
Fe_2ZrO_5-Fe_2O_3	0.77	1.65 mA cm^{-2}	27 (370 nm)	8
CeO_x-modified hematite	~0.65	0.6 mA cm^{-2}	~41 (350 nm)	9
α-Fe_2O_3/$MXene_{5/1}$ NRs	~0.9	1.1 mA cm^{-2}	10 (350 nm)	10
F-Ti-Fe_2O_3/Co(salen)	0.81	3.02 mA cm^{-2}	40 (360 nm)	11
Ti:α-Fe_2O_3-OH	~0.9	~0.9 mA cm^{-2}	~49 (400 nm)	12
Fe_2O_3 NT-FeOOH/NiOOH	~0.65	2.0 mA cm^{-2}	no	13
C-Co-Ti-Fe_2O_3	0.7	2.24 mA cm^{-2}	40 (370 nm)	14

References

1. Z. Luo, T. Wang, J. Zhang, C. Li, H. Li and J. Gong, *Angew. Chem. Int. Ed.*, 2017, **56**, 12878-12882.
2. X. Long, L. Gao, F. Li, Y. Hu, S. Wei, C. Wang, T. Wang, J. Jin and J. Ma, *Appl. Catal. B Environ.*, 2019, **257**, 117813.
3. F. Li, J. Li, L. Gao, Y. Hu, X. Long, S. Wei, C. Wang, J. Jin and J. Ma, *J. Mater. Chem. A*, 2018, **6**, 23478-23485.
4. N. S. Gajbhiye and S. Prasad, *Thermochim. Acta*, 1996, **285**, 325-336.
5. H. Bemana and S. Rashid-Nadimi, *Electrochim. Acta*, 2017, **229**, 396-403.
6. K. Wang, Y. Liu, K. Kawashima, X. Yang, X. Yin, F. Zhan, M. Liu, X. Qiu, W. Li, C. B. Mullins and J. Li, *Advanced Science*, 2020, **7**, 2002563.
7. M. P. Suryawanshi, U. V. Ghorpade, S. W. Shin, U. P. Suryawanshi, H. J. Shim, S. H. Kang and J. H. Kim, *Small*, 2018, **14**, 1801226.
8. T. Jiao, C. Lu, D. Zhang, K. Feng, S. Wang, Z. Kang and J. Zhong, *Appl. Catal. B Environ.*, 2020, **269**, 118768.
9. M. G. Ahmed, M. Zhang, Y. F. Tay, S. Y. Chiam and L. H. Wong, *ChemSusChem*, 2020, **13**, 5489-5496.
10. R.-K. Ye, S.-S. Sun, L.-Q. He, S.-R. Yang, X.-Q. Liu, M.-D. Li, P.-P. Fang and J.-Q. Hu, *Appl. Catal. B Environ.*, 2021, **291**, 120107.
11. R. Wang, Y. Kuwahara, K. Mori, C. Louis, Y. Bu and H. Yamashita, *J. Mater. Chem. A*, 2020, **8**, 21613-21622.
12. X. Zhang, X. Wang, X. Yi, J. Ye and D. Wang, *ACS Sustainable Chemistry & Engineering*, 2019, **7**, 5420-5429.
13. C. Feng, S. Fu, W. Wang, Y. Zhang and Y. Bi, *Appl. Catal. B Environ.*, 2019, **257**, 117900.
14. H. Lan, Y. Xia, K. Feng, A. Wei, Z. Kang and J. Zhong, *Appl. Catal. B Environ.*, 2019, **258**, 117962.